NJC

Accepted Manuscript

This is an *Accepted Manuscript*, which has been through the Royal Society of Chemistry peer review process and has been accepted for publication.

Accepted Manuscripts are published online shortly after acceptance, before technical editing, formatting and proof reading. Using this free service, authors can make their results available to the community, in citable form, before we publish the edited article. We will replace this *Accepted Manuscript* with the edited and formatted *Advance Article* as soon as it is available.

You can find more information about *Accepted Manuscripts* in the Information for Authors.

Please note that technical editing may introduce minor changes to the text and/or graphics, which may alter content. The journal's standard Terms & Conditions and the Ethical guidelines still apply. In no event shall the Royal Society of Chemistry be held responsible for any errors or omissions in this *Accepted Manuscript* or any consequences arising from the use of any information it contains.

ROYAL SOCIETY OF CHEMISTRY

www.rsc.org/njc

A Sonochemical approach for the synthesis of thermally stable mesoporous microspheres of TiO_2 for use as high performance anode for Li-ion batteries

Satyendar Sunkara[a], N. Munichandraiah[b], K.B.R. Varma[a], S.A. Shivashankar[a,c]

[a]Materials Research Centre, [b]Department of Inorganic and Physical Chemistry, [c]Centre for Nano Science and Engineering, Indian Institute of Science, Bengaluru-560012, India

Abstract

A facile, surfactant-free sonochemical synthesis route at a relatively low temperature was employed to prepare mesoporous, microspheres of anatase titanium dioxide (TiO_2), using the heteroleptic (mixed-ligand) complex, bis-isopropoxy-bis-tertiarybutylacetoacetatotitanium, $[Ti(O^iPr)_2(tbaoac)_2]$, as precursor. The transformation of as-prepared material into crystalline TiO_2 was achieved by heating in air at 500^o C. Interestingly, the material retained its pure anatase phase even after heating at 800^o C. The as-prepared sample and the heated ones were characterized by powder X-ray diffraction (PXRD), X-ray photoelectron spectroscopy (XPS), and electron microscopy (SEM, TEM) which, together, revealed that the spheres are mesoporous and, significantly, hollow. As anode material in the Li-ion battery, the titania microspheres exhibited a high reversible capacity of 212 $mAhg^{-1}$ after 100 charge and discharge cycles and displayed excellent cycling stability.

1. Introduction

Due to its favourable physico-chemical properties, titanium dioxide (TiO_2) has been studied extensively as a prospective material in the context of photocatalysis[1,2,3,4,5,6], dye-sensitized solar cells[7,8,9], sensing[10], photo-electrochemical (PEC) water splitting[11,12] and Li-

ion batteries (LIBs)[13,14,15,16]. Furthermore, TiO_2 also has the advantages of low cost (due to its abundance) and low toxicity, and superior chemical stability[17,18,19]. Among the different polymorphs of TiO_2 - brookite, rutile, anatase, and TiO_2 (B) - anatase TiO_2 has been investigated extensively as the anode material for LIBs[14,15,20-22]. In the crystal structure of anatase, each Ti atom coordinates with six oxygen atoms forming TiO_6 octahedra, leading to a three-dimensional framework providing favourable empty sites for the process of lithium intercalation and deintercalation[21]. Anatase titania accommodates '0.1 to 1.0' Li ions per TiO_2 unit[22,23] with an average operating potential (lithium insertion/extraction) of ~ 1.8 V. Although the high operating voltage does not offer high power density, TiO_2 is a safe electrode material as it prevents the formation of a solid electrolyte interface (SEI) and, thus, prevents the electroplating of lithium at high current densities.

LIBs continue to be investigated by many researchers because of their high energy density (resulting in their widespread use in portable electronics), power density, long life span and environmental benignity[24,25,26]. Intrinsic properties such as morphology, specific surface area, and pore size distribution of the electrode material affect the electrochemical performance of LIBs. To overcome various challenges pertaining to LIBs, different materials structured to be mesoporous, such as iron oxide[27,28], cobalt oxide (Co_3O_4) [29,30]and manganese oxide[31,32], have been developed so as to meet the aforementioned requirements of an effective electrode material. But most of these oxide structures undergo local stress during electrochemical cycling (charge/discharge) and lose structural integrity. In addition, the low electrical conductivity of these materials causes poor rate capability and limits their practical application. Although the electrical conductivity of TiO_2 is rather low, it has been demonstrated that mesoporous titania displays modest but appreciable electrochemical performance, while maintaining structural integrity upon lithium cycling[33,34].

Generally, porous structures are synthesized by template-based methods, including hard and soft templates. The pathways for removing the (organic) templates to obtain the final product are thermal annealing, acid leaching, or treatment in an organic solvent or alkali solution[35]. Thermal treatment usually leads to an increase in the grain size and causes the framework of the mesoporous structure to collapse, leading eventually to reduction in the specific surface area. Furthermore, conventional synthesis of the mesoporous structures requires specially designed autoclaves and long durations, sometimes as much as several days. On the other hand, the sonochemical technique has proven to be a versatile technique to synthesize novel materials, as it shortens the synthesis duration considerably and is environmentally benign[36,37]. In sonochemical synthesis, chemical reactions can occur when a solution containing reactants is subjected to powerful ultrasonic irradiation. The reaction mechanisms involved in sonochemistry have been explained well in previous reports[38,39]. The formation, growth, and implosive collapse of bubbles in the solvent due to application of powerful ultrasound generate local temperatures and pressures of about 5000 K and 1800 atm, respectively[38,39]. Wang et al. reported the synthesis of mesoporous TiO_2 by sonochemistry using octadecylamine as the structure-directing agent and titanium isopropoxide (TIP) as the precursor[40]. But the hygroscopic nature of TIP is a limitation to this method.

Unlike in the previous approaches referred to above, we report a novel strategy that is benign, rapid, and surfactant-free for the synthesis of thermally stable mesoporous microspheres of TiO_2 using the heteroleptic titanium precursor, bis-isopropoxy-bis-tertiarybutylacetoacta- tetitanium [Ti $(O^iPr)_2(tbaoac)_2$, where tbaoac= tertiarybutylacetoacetate].

2. Experimental Section

All chemicals used in the synthesis were of the AR grade. Absolute ethanol, titanium (IV) isopro-xide (97 %, Sigma-Aldrich) and tert-butyl acetoacetate (Alfa-aesar) were used as received, without further purification.

2.1 Synthesis of TiO_2

The precursor $Ti(O^iPr)_2(tbaoac)_2$ was synthesised using the procedure reported in the literature[41]. The as-prepared precursor, which is in powder form (0.5 g), was dissolved in 50 ml of ethanol in a glass vessel. The solution was placed in an ice bath and subjected to sonication for 60 min using an ultrasonic processor (SONIC Model VCX 500, 500 Watts) operating at 20 kHz, equipped with a high-intensity solid Ti probe (13 mm dia). The amplitude of ultrasonic waves was kept at 40% of the maximum, with a duty cycle of 66% (ON for 2 s, OFF for 1 s). The ice bath prevents overheating of the reaction solution. The resulting powder was collected by centrifugation, washed several times with deionized water and finally with ethanol, and oven-dried in air at 60^{o}C for 12 hours. The powder product was found to be amorphous and was heated in air in a muffle furnace at 500^{o}C for 2 h to remove the organic byproducts formed during the synthesis and to obtain crystalline TiO_2. In addition, some of the as-prepared powder was also heated in air at 800^{o}C. The sample that was heated at 500^{o}C was investigated in detail for its potential application as anode material for Li-ion batteries.

2.2 Sample Characterization

X-ray powder diffraction (XRD) data were collected using Cu K_α radiation (PANalytical X'Pert PRO). The morphology of samples was examined by a field-emission scanning electron microscope (FESEM, Carl Zeiss ULTRA 55). A high-resolution transmission electron microscope (HRTEM, JEOL JEM-2100F) operating at 200 kV was used for structural investigations. Raman spectroscopy and photoluminescence measurements were

carried out with laser excitation at 514 nm and 325 nm, respectively (Horiba Jobin-Yvon LabRAM HR100). Thermogravimetric analysis was (TGA) conducted to estimate the temperature at which the as-prepared (amorphous) sample was to be treated to obtain well-crystallised material (Netzsch Thermal Analyser). TGA was also used to estimate the decomposition temperature of the precursor. Diffuse-reflectance measurements were carried out in a spectrophotometer to determine the optical band gap of TiO_2 (Perkin-Elmer Lambda 750). The specific surface area and pore size distribution in the samples were measured by the Brunauer–Emmett–Teller (BET) method (Micrometrics ASAP2020). The chemical nature of the powder samples was examined by X-ray photoelectron spectroscopy using Al K_α radiation (1.486 keV, Axis Ultra DLD, Kratos Analytical).

2.3 Electrochemical Measurements

To fabricate electrodes for electrochemical measurements, the active material (TiO_2), acetylene black (AB, 99.9%, Alfa Aesar), polyvinylidene difluoride (PVDF, Aldrich) were mixed in the weight ratio of 7:2:1. A few drops of 1-methyl-2-pyrrolidinone (NMP, 99%, Aldrich) were added to the mixture to obtain slurry, with which copper disks 12 mm in diameter were coated and vacuum-dried at 110^{o}C for 12 h. The mass of active material was ~2.5 mg cm^{-2}. The electrolyte employed was 1M $LiPF_6$ dissolved in ethylene carbonate, diethyl carbonate and dimethyl carbonate (2:1:2 v/v, Chameleon). Lithium metal foil of thickness 0.75 mm (99.9%, Aldrich) was used as both the counter- and reference electrode, and Celgard porous polypropylene membrane (2400) was used as separator. Coin cells (CR2032, Hohsen Corporation, Japan) were assembled in argon ambient in a glove box (MBraun model Unilab). Cyclic voltammetry, impedance measurements, galvanostatic charge–discharge, and rate capability measurements were conducted using a battery tester (Solartron Modulab).

3. Results and Discussion

Mesoporous microspheres of TiO_2 were prepared by sonochemical synthesis route followed by heat treatment in air at 500°C. The XRD patterns of the as-prepared powder and the powder heated at 500°C and 800°Care shown in Fig.1. As noted already, the as-prepared powder was found to be amorphous. All the peaks present in the XRD patterns of samples heated at 500°C and 800°C can be indexed to the tetragonal structure of TiO_2 (JCPDS No. 21-1272), illustrating that these samples

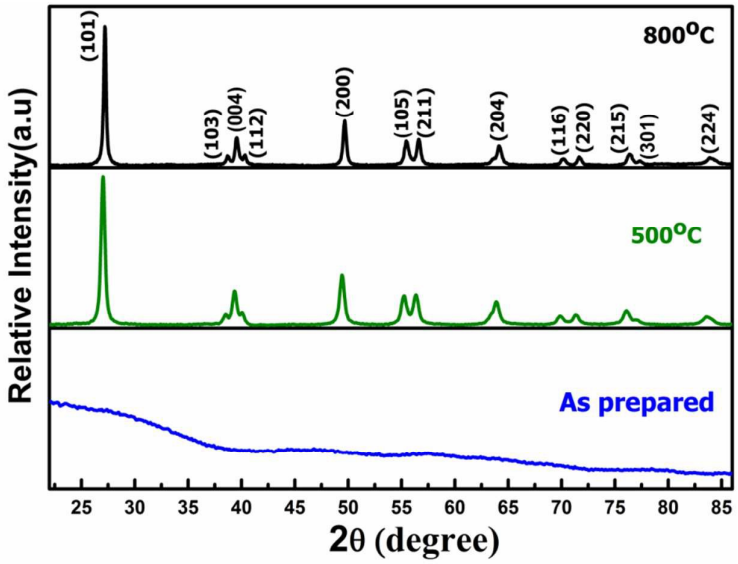

Fig. **1** X-ray diffraction (XRD) patterns of as prepared powder and powder heated at 500°C and 800°C

comprise the anatase phase; no peaks corresponding to the other polymorphs of TiO_2 are present. In general, the phase transition from anatase to rutile takes place at temperatures above 500°C (in air) and anatase converts completely to the rutile phase at 800°C. But it is seen in the present case that, even after heating in air at 800°C, the anatase phase of TiO_2 did not transform to the rutile phase, demonstrating clearly the thermal stability of anatase TiO_2 prepared as described above. A similar behaviour has been reported in the case of doped

TiO_2[42]. The persistence of the anatase phase up to 800°C in the present samples meritsfurther investigation. The thermal behaviour of the as-prepared material was examined of by thermogravimetric analysis (TGA) in air at a ramp rate of 10° C per minute and the results are displayed in Fig **S1** of supplementary information. The TGA data show a multi-step weight loss in the temperature range of 100-350°C, with no significant loss at higher temperatures. The initial weight loss of 15 % in the 100-200°C range is attributed to the loss of adsorbed water and organic moieties. The second stage of weight loss is due to the crystallization of anatase titania. Based on the TGA data and previous reports, it was decided to carry out heating (in air) of the as-prepared material at 500°C to obtain anatase TiO_2.

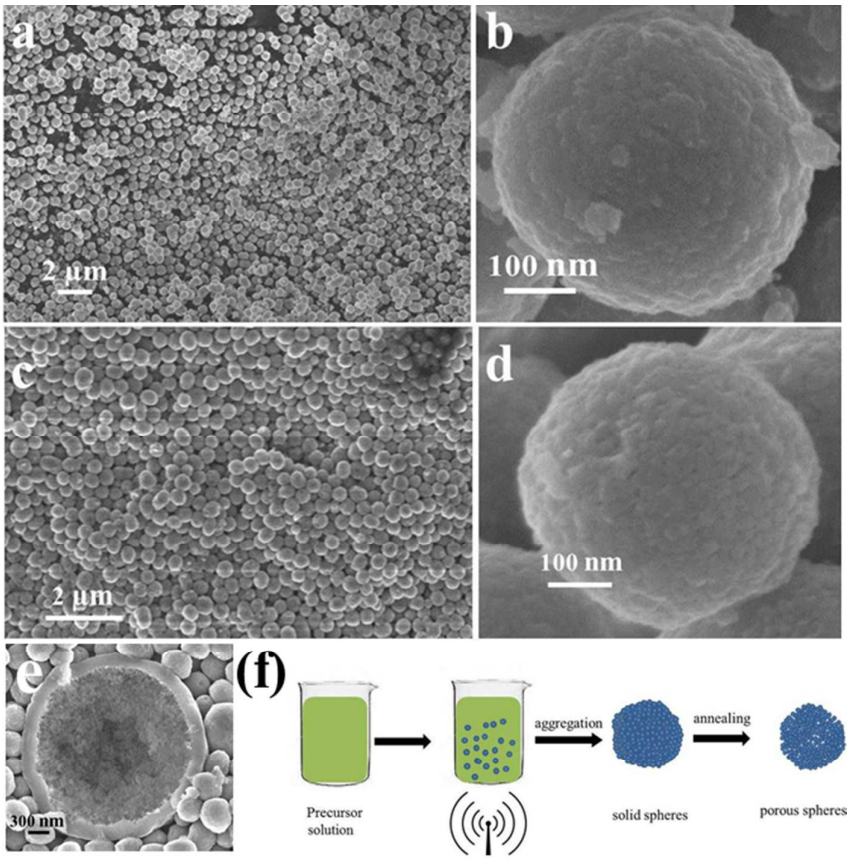

Fig. **2** Low- and high-magnification FESEM images of as-prepared powder (a and b); powder heated at 500°C (c and d); a representative broken sphere, revealing its hollowness (e); and schematic representation of growth mechanism (2f).

The morphology of the as-synthesized and heated samples was investigated by SEM. The low-magnification image of titania of Fig.**2a** reveals that the as-prepared sample is comprised of nearly monodisperse spheres with an average size of 500 nm in diameter. Fig. **2b** depicts the close-up (high-magnification) image of an individual sphere, which reveals that it is comprised of many nanoparticles. Figures **2c** and **2d** respectively represent the low- and high- magnification images of the sample heated at 500^{o}C. The images reveal that, due to the loss of organic moieties, the microspheres have shrunk in size (by about 20-30 nm). The

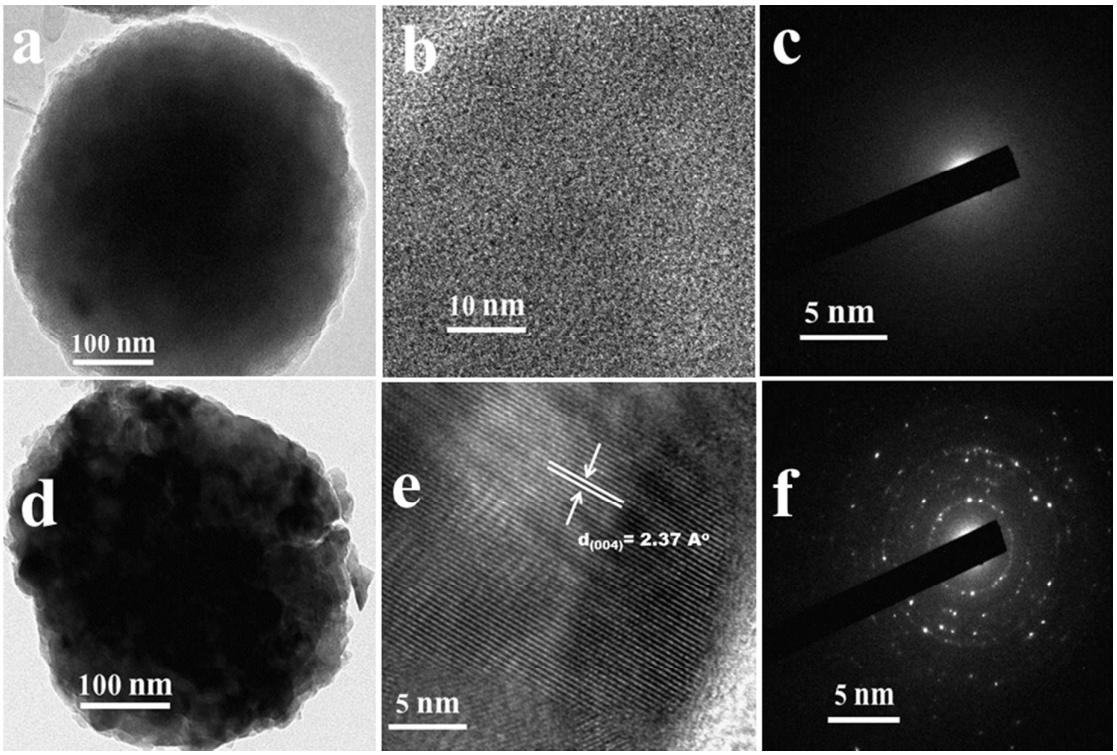

Fig.**3** TEM, HRTEM, SAED images of the as-prepared amorphous TiO_2 (a, b and c); and anatase TiO_2 obtained by heating in air at 500^{o}C (d, e and f)

high magnification image in Fig. **2d** evidences that heat treatment renders the spheres porous. The image in Fig.**2e** shows a broken sphere, which demonstrates that the heated spheres are hollow and that the surface of the spheres is composed of very tiny particles. Reduction in total surface energy is the driving force behind the spherical shape of the particles. The

schematic of the mechanism proposed for the formation of the mesoporous microspheres is shown in Fig. **2f**.

To obtain further insight into the morphology of the as-synthesized and heated titania, TEM analysis was carried out. The TEM images of a single sphere from the as-prepared and heated samples are shown in Fig. **3a** and **3d**, respectively. The images are consistent with those obtained by SEM: pores can be readily discerned in the heated sample. The HRTEM image and selected-area electron diffraction (SAED) of the as-prepared sample (Fig. **3b** and **3c**, respectively) confirm that the sample is amorphous. The HRTEM image of the heated sample (Fig. **3e**) contains distinct lattice fringes with *d* spacing of 2.37 Å and 2.43 Å, corresponding to the lattice planes (004) and (103), respectively. The SAED pattern of the heated sample features bright rings that are consistent with the polycrystalline nature of the sample.

The phase purity of the titania was examined also by Raman spectroscopy; the Raman spectrum of the sample heated at 500^{o}C is shown in Fig. **4**. The peaks centred at 145 cm^{-1}, 196 cm^{-1}, 639 cm^{-1} may be assigned to the E_g modes of vibration, and those at 397 cm^{-1} and 516 cm^{-1} to the B_{1g} modes of vibration[43]. The absence of any peaks attributable to the other polymorphs of TiO_2 demonstrates the phase purity of the anatase TiO_2 prepared as described above. Room-temperature photoluminescence (PL) spectrum of the sample heated at 500^{o}C was obtained using laser excitation at 325 nm (Fig.S2 of supplementary information). According to the literature, the PL spectrum of anatase TiO_2 shows two intense peaks, one at 388 nm and another in the range of 400-600 nm of wavelength[44]. The one about 388 nm is called near-band-gap emission (NBE), contributed by the excitation of electrons from valence band to the conduction band. The feature in the range of 400-600 nm is broad-band emission (BBE) and is attributed to defects inside the material, such as titanium vacancies, titanium

interstitials, oxygen vacancies, and oxygen interstitials. The relative intensity of NBE and BBE reflects the degree of crystalline perfection.The PL spectrum of Fig. **S2** shows that the PL spectrum of the present anatase TiO_2 contains only one intense peak around 550 nm, corresponding to BBE. The reason for not observing NBE may be the high concentration of defects in sample.

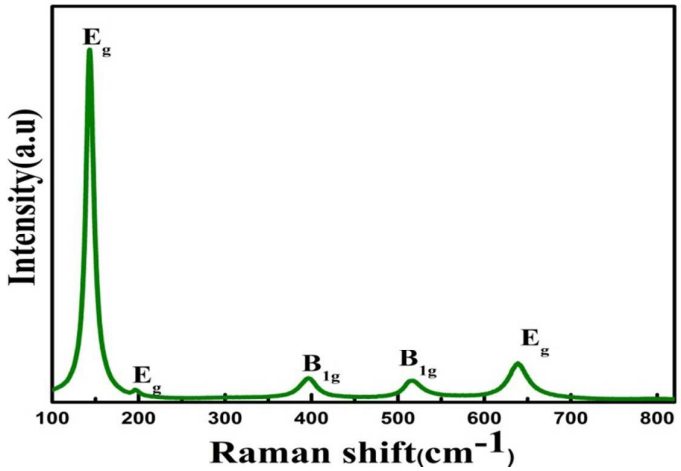

Fig. **4** Raman spectrum of anatase TiO_2 microspheres

The optical band gap of TiO_2 was determined by UV-visible spectroscopy. Fig. **5a** displays the UV-visible diffuse reflectance spectrum of TiO_2 microspheres, illustrating moderate light absorption in the visible region of the spectrum. The plot of the Kubelka–Munk function *versus* the energy of the photons absorbed (Fig.**5b**) allows the calculation of the band gap of TiO_2 comprised of microspheres. From the figure, the band gap of TiO_2 is extrapolated to 3.09 eV, which is considerably lower than the band gap reported for "standard" anatase TiO_2 (3.3 eV). It is surmised that the smaller band gap measured in the present sample is attributable to lattice defects (cf. the PL spectrum) and the hollowness of the spheres.

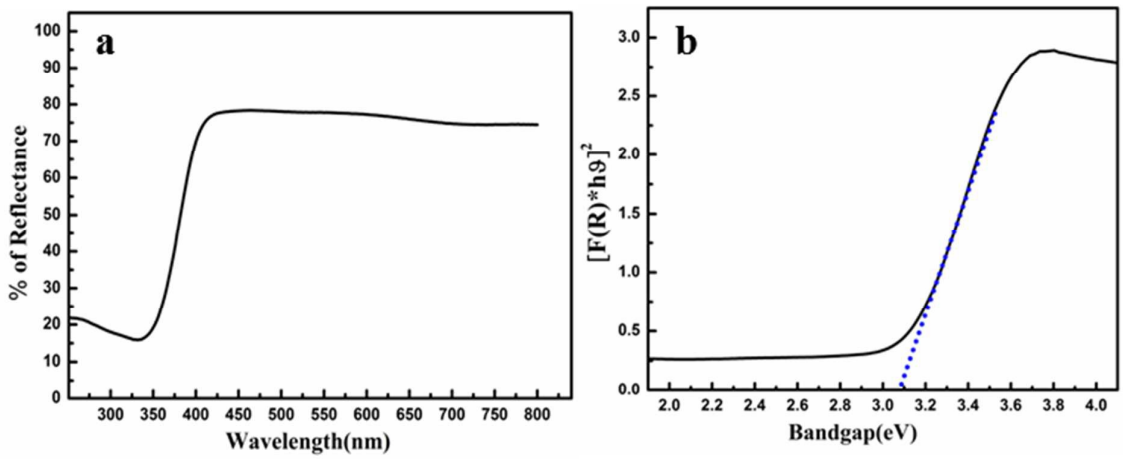

Fig.5 UV-visible diffuse reflectance spectra (a); Kubelka–Munk function plot of the anatase TiO_2 microspheres (b)

X-ray photoelectron spectroscopic (XPS) analysis was carried out to examine the oxidation state and chemical composition of TiO_2. Fig. **S3** of supplementary information shows the normalized Ti 2p and O 1s core level XPS spectra. The core level spectrum of Ti *2*p (Fig. **S3 a**) contains two broad peaks centred at ~465.1 eV and ~459.4 eV, which are characteristic of Ti $2p_{1/2}$ and Ti $2p_{3/2}$ in Ti^{+4}, respectively[45,46]. The normalized core level XPS spectrum of O 1s (Fig. **S3b**) exhibits two characteristic peaks at 529.4 eV and 530.9 eV that can be assigned to Ti-O-Ti and Ti−OH, respectively[47]. The difference between the binding energies of Ti-O-Ti and Ti-OH was found to be 1.5 eV, which is in good agreement with the value that has been reported in the literature[48].

A high specific surface area and porous morphology of the electrode material are essential to achieving superior electrochemical performance. High surface area enhances the contact area of the electrode with the electrolyte and leads to higher conductivity. Porous morphology can provide a greater degree of contact between the electrode and the electrolyte, as well as help accommodate the volume changes that occur during the charging and discharging processes. To determine the specific surface area of the sample (heated at 500^{o}C) and the distribution of pore sizes in it, N_2 gas adsorption–desorption measurements were carried out

at 77 K and the results are reported in Fig. **6**. The isotherm of Fig.**6** is a N_2 adsorption isotherm of type IV, signifying that the structure is mesoporous. The BET specific surface area of the sample is 59.4 $m^2 g^{-1}$. The Barrett–Joyner–Halenda (BJH) pore-size distribution plot shown in inset of Fig.**6** reveals that the peak of the pore size distribution is at 3.3 nm and the average pore size is in the range of 3-4 nm.

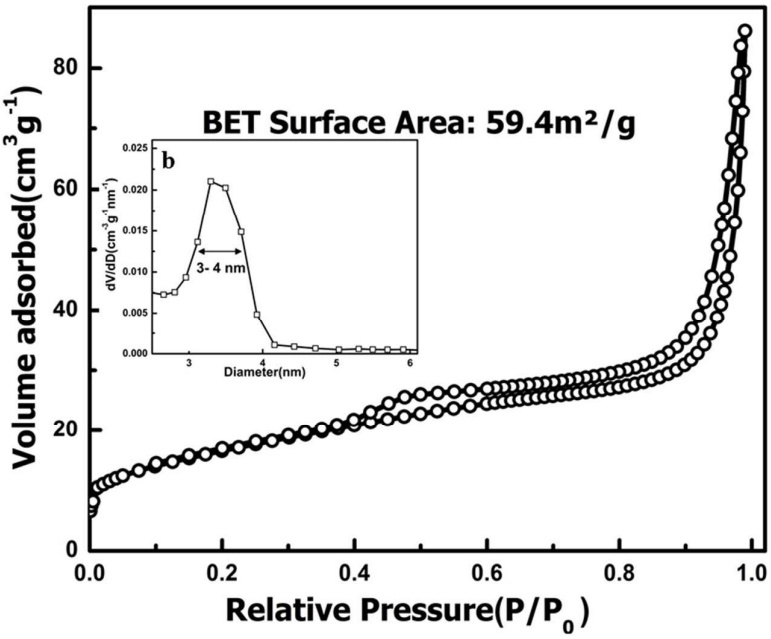

Fig. **6** N_2 adsorption–desorption isotherm of TiO_2 microspheres, and pore size distribution (inset)

The electrochemical properties of TiO_2 were evaluated by cyclic voltammetry (CV). Fig. **7** shows the CV curves of TiO_2 in the voltage range of 1.0-3.0 V, obtained at a scan rate of 0.1 mV s^{-1}. The electrochemical reaction taking place may be described by the following equation[49,50].

$$TiO_2 + xLi + x\,e^- \leftrightarrow Li_xTiO_2 \text{ (where } x=0.5) \quad (1)$$

According to literature, the broad peak at 1.71 V in the first cathodic scan is assignable to lithium insertion and to the crystal structure transition between tetragonal TiO_2 and orthorhombic Li_xTiO_2, where 'x' is the insertion coefficient[50]. From the second cycle, the peaks are found to remain the same except that the intensity of the peaks changes. In the anodic part of the scan cycle, the peak at 2.03 V corresponds to the delithiation process and signifies the reversibility of delithiation[51].

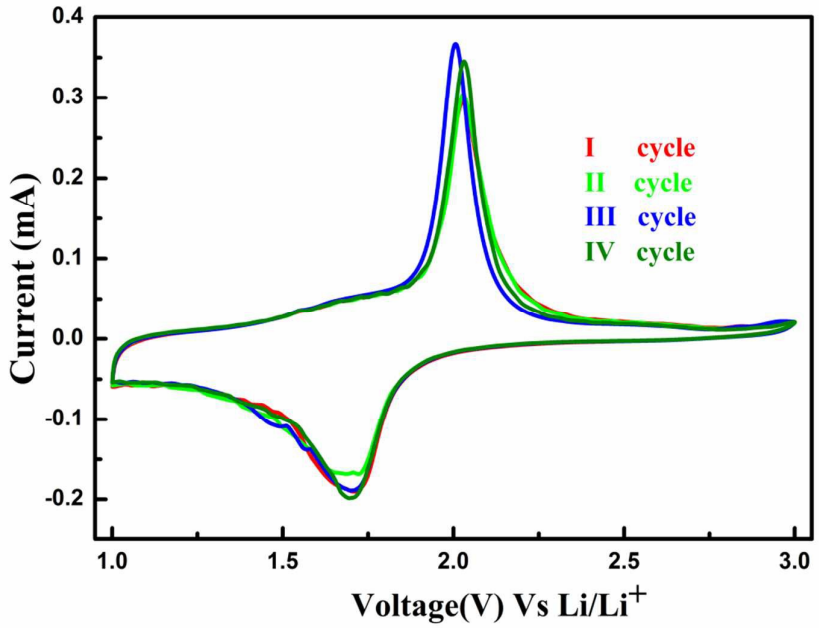

Fig. 7 CV curves at a scanning rate of 0.1 mV s^{-1} in the voltage range of 1.0–3.0 V.

Fig.**8** shows the potential profile of the TiO_2 electrode in the 1st, 2nd and 100th charge-discharge cycles at a current density of 85 mA g^{-1} (0.25 C, where 1 C=335 mA g^{-1}), in the potential range of 1.0 – 3.0 V *vs.* Li/Li^+. A large gap between charge and discharge curves is seen, which is assignable to the poor electrical conductivity of the electrode material[52]. The initial charge and discharge capacities obtained from these data are 261.7 and 233.1 mA h g^{-1}, respectively, which are higher than the theoretical values for TiO_2. These higher capacities are attributable to the formation of a solid electrolyte interphase (SEI) layer due to decomposition of the electrolyte. The charge and discharge capacities deduced from the

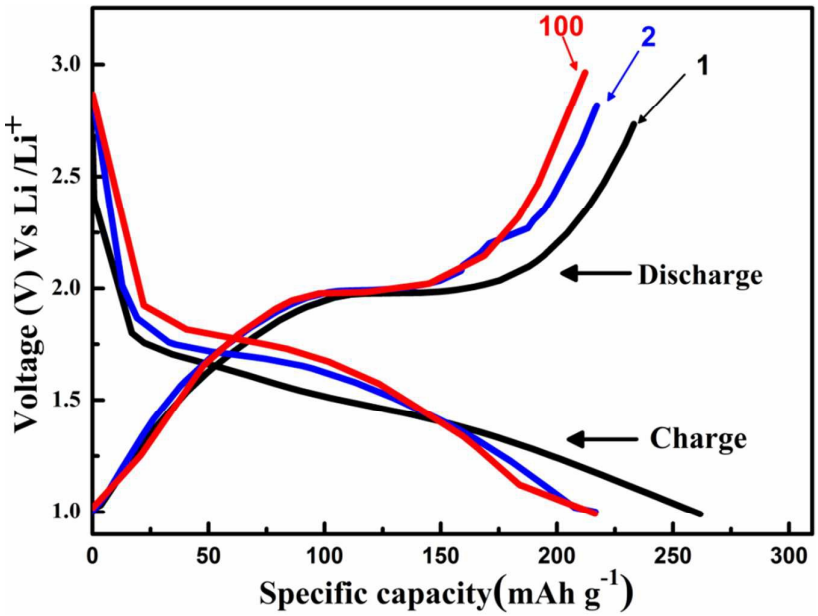

Fig. 8 Galvanostatic charge–discharge profiles at a current rate of 0.25 C

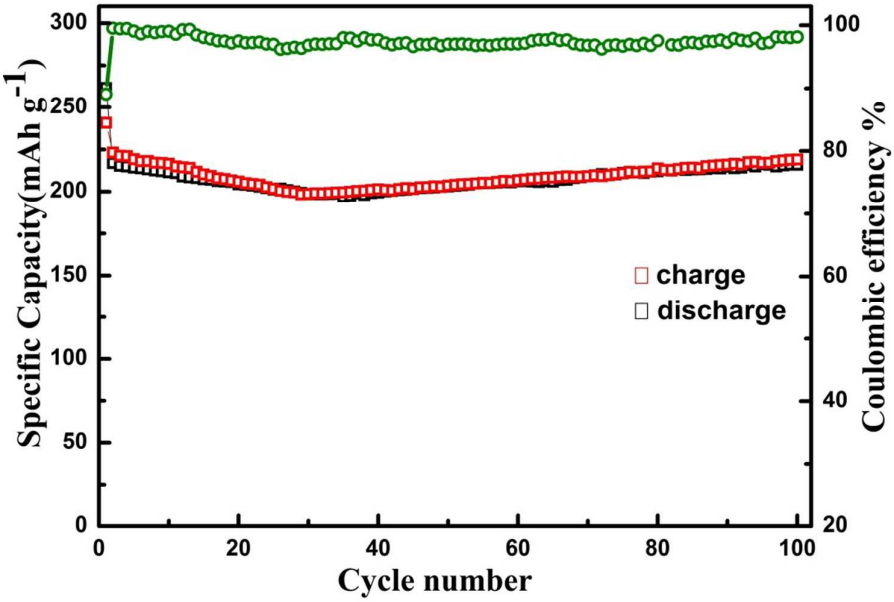

Fig. 9 Cycling performance and coulombic efficiency at a current rate of 0.25 C

second cycle are 217.1 and 216.5 mA h g^{-1}, respectively, and the calculated coulombic efficiency is 99.7%. The discharge capacity continues to decrease slightly up to 30 cycles and the discharge capacity obtained at the end of 30 cycles is 192.2 mA h g^{-1}. Beyond 30 cycles, very interestingly, the discharge capacity increases slowly and a capacity of 212.3 mA h g^{-1} is of obtained after the 100^{th} cycle, with a coulombic efficiency 98%. This unusual phenomenon

is similar to the one reported[53] in the case of $CoMn_2O_4$. This is attributed to the electrochemical activation of the "inner part" of the electrode due to penetration of electrolyte into the core of the microspheres, whereupon charge and discharge take place at low current rates. The high discharge capacity obtained even after 100 cycles of charge and discharge illustrates the excellent cycling stability of the TiO_2 electrode. Cycling performance and coulombic efficiency of the electrode material at a current rate of 0.25C is shown in Fig. **9**. The coulombic efficiency is close to 98% up to 100 cycles at a current rate of 0.25C, which illustrates the superior performance of the present anatase material as the anode in LIBs.

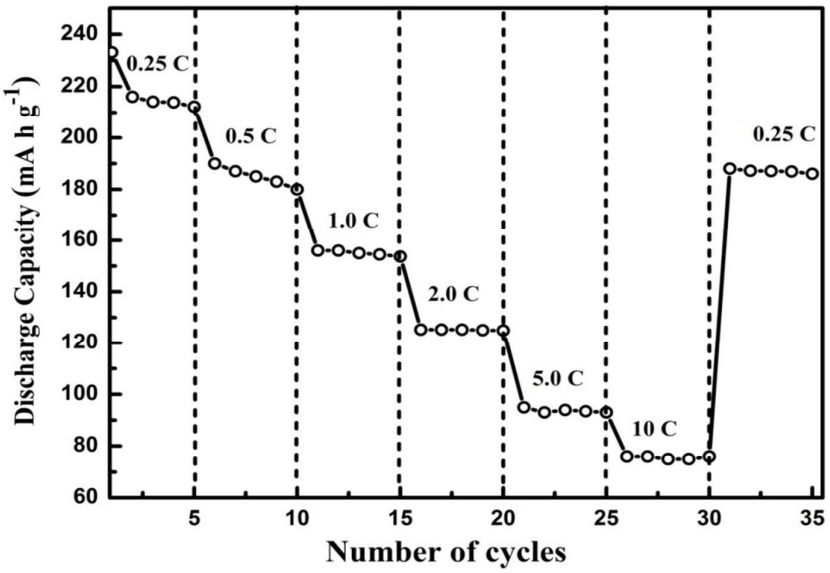

Fig. **10** Rate capability of TiO_2 electrode at different current rates

The application of the present anatase material for charging and discharging at high current rates has also been investigated. Fig. **10** displays the rate capability of the TiO_2 electrode at various current rates (0.25, 0.5, 1.0, 2.0, 5.0, 10C, where 1C=335 mA g^{-1}). The electrode delivered discharge capacities of 190, 156, 125.3, 95, 76 mA h g^{-1} at the currents rates of 0.5, 1.0, 2.0, 5.0, 10C, respectively, establishing the good rate capability of the anatase electrode. A specific discharge capacity of 188.5 mA h g^{-1} is obtained when the current is reverted back to 0.25C.

To evaluate the transport kinetics of the anatase electrode material, AC impendence measurements were carried under open-circuit conditions and also after 100 charge/discharge cycles at a current rate of 0.25C. The Nyquist plot (Fig. **11**) shows a depressed semicircle in the high- and medium-frequency ranges. The semicircle in the mid-frequency range may be assigned to the charge-transfer resistance (R_{ct}) and, in the high frequency range, is attributable to the resistance of electrolyte (R_s). The straight line in the low frequency side is assigned to the Warburg impedance (Z_w). R_{ct} relates to charge transfer through the electrode–electrolyte interface and Z_w relates to solid state diffusion of Li^+. The inset of Fig.**11** shows Nyquist plots after 100 cycles of charge/discharge. It can be seen from the figure that there is a reduction in cell impedance with the anatase electrode, which is due to the pulverization process.

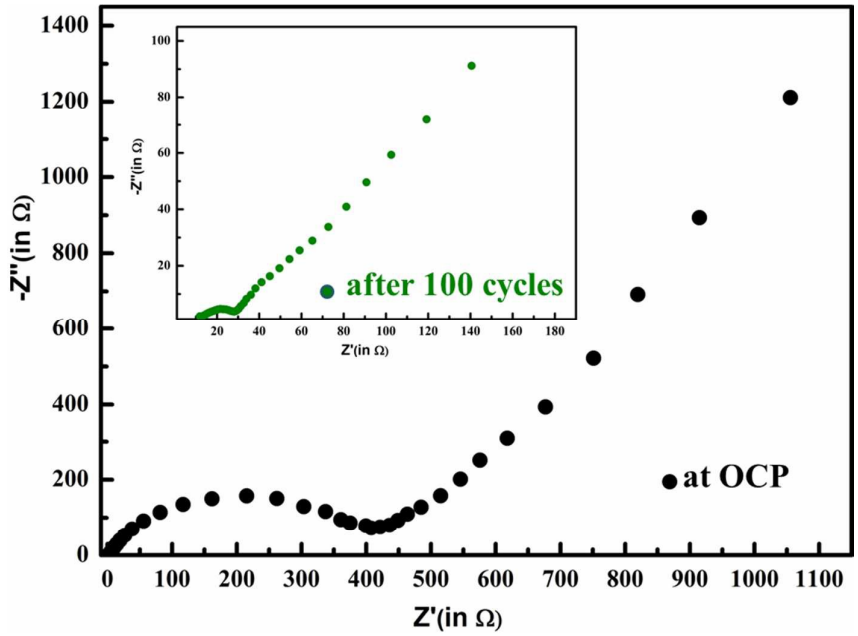

Fig. 11 Nyquist plots from electrochemical impedance spectroscopy for anatase TiO_2 electrode

The superior electrochemical performance of the mesoporous microspheres of the present anatase material could be attributed to the following factors. First, the porosity offers

a large-area material/electrolyte contact by shortening the diffusion length of the Li ion, whereas the relatively large specific surface area enhances the charge transfer rate[54]. Second, the hollow structures provide adequate "breathing space" for local volume expansion/contraction during charging/discharging and hence lead to long cycling life. The hollow structure also enhances specific capacity by providing extra space for the storage of Li ions. Investigations are under way to improve the electrochemical performance of the present material further.

4. Conclusions

Nearly monodisperse, thermally stable microspheres of titania of diameter ~500 nm were synthesized by the sonochemical process, using a heteroleptic (mixed-ligand) complex of titanium. After post-synthesis heating in air, phase-pure nanocrystalline anatase was obtained. When employed as the anode for Li-ion batteries, the anatase material obtained by heating in air at 500^{o}C exhibited a high discharge capacity, with excellent cycling stability. The material also showed a relatively good rate capability. Although the specific capacitance is low compared to other materials, it is reckoned that the present material can serve as a promising electrode material in some special applications that do not require high capacitance. The method of synthesis adopted in this effort is cost-effective and may be extended to other materials.

Acknowledgements

Satyendar Sunkara thanks Pradeep, Varadaraj, Prahlada, Bharathi.R, and Penki for their help sample characterization. S.S. also thanks MHRD, Govt. of India, for the award of a research fellowship. The authors thank CeNSE, IISc, for providing access to its facilities.

Notes and references

1 H. G. Yang, G. Liu, S. Z. Qiao, C. H. Sun, Y. G. Jin, S. C. Smith, J. Zou, H. M. Cheng and G. Q. (Max) Lu, *J. Am. Chem. Soc.*, 2009, **131**, 4078–4083.

2 S. Liu, J. Yu and M. Jaroniec, *J. Am. Chem. Soc.*, 2010, **132**, 11914–11916.

3 A. Fujshima and K. Honda, *Nature*, 1972, **238**, 37–38.

4 A. Kubacka, M. Fernández-García and G. Colón, *Chem. Rev.*, 2012, **112**, 1555–1614.

5 S. P. Albu, A. Ghicov, J. M. Macak, R. Hahn and P. Schmuki, *Nano Lett.*, 2007, **7**, 1286–1289.

6 A. Jena, R. Vinu, S. A. Shivashankar and G. Madras, *Ind. Eng. Chem. Res.*, 2010, **49**, 9636–9643.

7 X. Wu, G. Q. (Max) Lu and L. Wang, *Energy Environ. Sci.*, 2011, **4**, 3565–3572.

8 A. Hagfeldt, G. Boschloo, L. Sun, L. Kloo and H. Pettersson, *Chem. Rev.*, 2010, **110**, 6595–6663.

9 B. O'Regan and M. Graetzel, *Nature*, 1991, **353**, 737–740.

10 C. Wang, L. Yin, L. Zhang and R. Gao, *J. Phys. Chem. C*, 2010, **114**, 4408–4413.

11 G. Wang, H. Wang, Y. Ling, Y. Tang, X. Yang, R. C. Fitzmorris, C. Wang, J. Z. Zhang and Y. Li, *Nano Lett.*, 2011, **11**, 3026–3033.

12 J. H. Park, S. Kim and A. J. Bard, *Nano Lett.*, 2006, **6**, 24–28.

13 A. Kuhn, R. Amandi and F. García-Alvarado, *J. Power Sources*, 2001, **92**, 221–227.

14 A. R. Armstrong, G. Armstrong, J. Canales and P. G. Bruce, *Angew. Chemie Int. Ed.*, 2004, **43**, 2286–2288.

15 G. Sudant, E. Baudrin, D. Larcher and J.-M. Tarascon, *J. Mater. Chem.*, 2005, **15**, 1263–1269.

16 M. A. Reddy, M. S. Kishore, V. Pralong, V. Caignaert, U. V Varadaraju and B. Raveau, *Electrochem. Commun.*, 2006, **8**, 1299–1303.

17 H. Bin Wu, J. S. Chen, H. H. Hng and X. Wen (David) Lou, *Nanoscale*, 2012, **4**, 2526–2542.

18 Z. Yang, D. Choi, S. Kerisit, K. M. Rosso, D. Wang, J. Zhang, G. Graff and J. Liu, *J. Power Sources*, 2009, **192**, 588–598.

19 D. Deng, M. G. Kim, J. Y. Lee and J. Cho, *Energy Environ. Sci.*, 2009, **2**, 818–837.

20 P. G. Bruce, B. Scrosati and J.-M. Tarascon, *Angew. Chemie Int. Ed.*, 2008, **47**, 2930–2946.

21 S. Yoon and A. Manthiram, *J. Phys. Chem. C*, 2011, **115**, 9410–9416.

22 M. Wagemaker, G. J. Kearley, A. A. van Well, H. Mutka and F. M. Mulder, *J. Am. Chem. Soc.*, 2003, **125**, 840–848.

23 G. Nuspl, K. Yoshizawa and T. Yamabe, *J. Mater. Chem.*, 1997, **7**, 2529–2536.

24 L. Shen, B. Ding, P. Nie, G. Cao and X. Zhang, *Adv. Energy Mater.*, 2013, **3**, 1484–1489.

25 Y. Wang, H. J. Zhang, L. Lu, L. P. Stubbs, C. C. Wong and J. Lin, *ACS Nano*, 2010, **4**, 4753–4761.

26 L. Peng, H. Zhang, Y. Bai, Y. Zhang and Y. Wang, *Nanoscale*, 2015, **7**, 8758–8765.

27 W. Shi, J. Zhu, D. H. Sim, Y. Y. Tay, Z. Lu, X. Zhang, Y. Sharma, M. Srinivasan, H. Zhang, H. H. Hng and Q. Yan, *J. Mater. Chem.*, 2011, **21**, 3422–3427.

28 Y. Ma, C. Zhang, G. Ji and J. Y. Lee, *J. Mater. Chem.*, 2012, **22**, 7845–7850.

29 K. T. Nam, D.-W. Kim, P. J. Yoo, C.-Y. Chiang, N. Meethong, P. T. Hammond, Y.-M. Chiang and A. M. Belcher, *Science*, 2006, **312** , 885–888.

30 Y. Li, B. Tan and Y. Wu, *Nano Lett.*, 2008, **8**, 265–270.

31 Y. Qiu, G.-L. Xu, K. Yan, H. Sun, J. Xiao, S. Yang, S.-G. Sun, L. Jin and H. Deng, *J. Mater. Chem.*, 2011, **21**, 6346–6353.

32 H. Wang, L.-F. Cui, Y. Yang, H. Sanchez Casalongue, J. T. Robinson, Y. Liang, Y. Cui and H. Dai, *J. Am. Chem. Soc.*, 2010, **132**, 13978–13980.

33 Y. Ren, L. J. Hardwick and P. G. Bruce, *Angew. Chemie Int. Ed.*, 2010, **49**, 2570–2574.

34 K. Wang, M. Wei, M. A. Morris, H. Zhou and J. D. Holmes, *Adv. Mater.*, 2007, **19**, 3016–3020.

35 J. Wang, Y. Zhou, Y. Hu, R. O'Hayre and Z. Shao, *J. Phys. Chem. C*, 2011, **115**, 2529–2536.

36 L. Zhang and J. C. Yu, *Chem. Commun.*, 2003, 2078–2079.

37 M. I. Dar and S. A. Shivashankar, *Mater. Res. Express*, 2014, **1**, 15025.

38 K. S. Suslick, *Sci.* , 1990, **247** , 1439–1445.

39 E. B. Flint and K. S. Suslick, *Science*, 1991, **253** , 1397–1399.

40 Y. Wang, X. Tang, L. Yin, W. Huang, Y. Rosenfeld Hacohen and A. Gedanken, *Adv. Mater.*, 2000, **12**, 1183–1186.

41 R. Bhakta, F. Hipler, A. Devi, S. Regnery, P. Ehrhart and R. Waser, *Chem. Vap. Depos.*, 2003, **9**, 295–298.

42 M. Hirano, C. Nakahara, K. Ota, O. Tanaike and M. Inagaki, *J. Solid State Chem.*, 2003, **170**, 39–47.

43 V. Swamy, A. Kuznetsov, L. S. Dubrovinsky, R. A. Caruso, D. G. Shchukin and B. C. Muddle, *Phys. Rev. B*, 2005, **71**, 184302.

44 Y.-H. Chang, C.-M. Liu, C. Chen and H.-E. Cheng, *J. Electrochem. Soc.* , 2012, **159** , D401–D405.

45 X. Chen, L. Liu, P. Y. Yu and S. S. Mao, *Science*, 2011, **331** , 746–750.

46 X. Lu, G. Wang, T. Zhai, M. Yu, J. Gan, Y. Tong and Y. Li, *Nano Lett.*, 2012, **12**, 1690–1696.

47 B. Erdem, R. A. Hunsicker, G. W. Simmons, E. D. Sudol, V. L. Dimonie and M. S. El-Aasser, *Langmuir*, 2001, **17**, 2664–2669.

48 X. Lu, D. Zheng, T. Zhai, Z. Liu, Y. Huang, S. Xie and Y. Tong, *Energy Environ. Sci.*, 2011, **4**, 2915–2921.

49 H. Lindström, S. Södergren, A. Solbrand, H. Rensmo, J. Hjelm, A. Hagfeldt and S.-E. Lindquist, *J. Phys. Chem. B*, 1997, **101**, 7717–7722.

50 G. Kim, C. Jo, W. Kim, J. Chun, S. Yoon, J. Lee and W. Choi, *Energy Environ. Sci.*, 2013, **6**, 2932–2938.

51 Y. J. Mai, X. H. Xia, R. Chen, C. D. Gu, X. L. Wang and J. P. Tu, *Electrochim. Acta*, 2012, **67**, 73–78.

52 C. Jiang, M. Wei, Z. Qi, T. Kudo, I. Honma and H. Zhou, *J. Power Sources*, 2007, **166**, 239–243.

53 L. Hu, H. Zhong, X. Zheng, Y. Huang, P. Zhang and Q. Chen, *Sci. Rep.*, 2012, **2**.

54 D. Liu and G. Cao, *Energy Environ. Sci.*, 2010, **3**, 1218–1237.

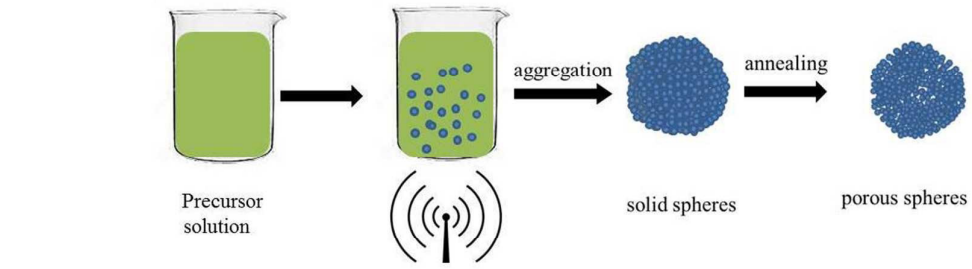

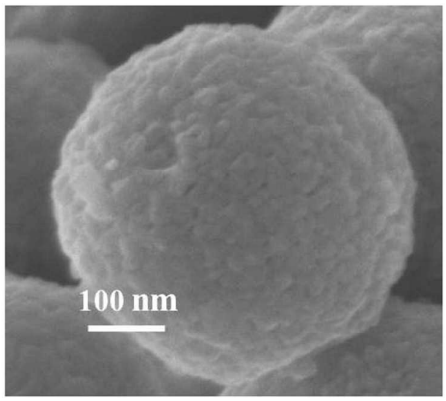

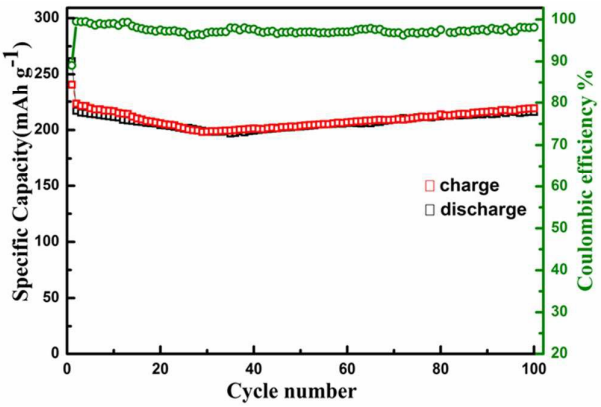

Microspheres of anatase TiO_2 exhibiting excellent cycling stability as anode material for Li-ion batteries have been prepared by sonochemical synthesis.